Simulation-driven Thermal Analyses for Cultural Heritage Conservation

Oscar Roman [1,2], Elisa Mariarosaria Farella[2], Fabio Remondino[2]

[1] Department Information Engineering and Computer Science (IECS), Program in Industrial Innovation - University of Trento, Trento, Italy - oscar.roman@unitn.it

[2] 3D Optical Metrology (3DOM) unit, Bruno Kessler Foundation (FBK), Trento, Italy - web: http://3dom.fbk.eu
email: oroman@fbk.eu, elifarella@fbk.eu, remondino@fbk.eu

Keywords: Cultural Heritage, Deep-Learning, Energy Simulations, Mesh-based FEM Simulation, Object Detection.

Abstract

Heritage masonry structures, with their complex geometries and variety of materials, pose significant challenges for accurate digital modelling and simulations for restoration and conservation purposes. In addition, traditional cultural heritage (CH) documentation workflows typically rely on geometric 3D acquisitions, often without supporting material diagnostics or structural insights. This work addresses this gap by introducing a data-driven workflow that leverages image-based information and 3D point clouds to extract both geometric and material-related attributes for energy analysis applications. The proposed methodology leverages Deep Learning (DL) and Finite Element Method (FEM) modelling to support energy simulation for cultural heritage assets. The proposed workflow integrates orthoimages and 3D data to segment masonry textures, estimate wall thickness, and generate a semantically enriched mesh tailored for energy analyses. A YOLO-based model identifies stone and mortar regions in high-resolution imagery, while point cloud voxelization and plane fitting are used to compute local thickness values. This information feeds into an adaptive meshing strategy, where mesh resolution is adjusted based on material texture and geometric features. A tunable parameter β enables control over mesh density, allowing for optimization of computational performance in thermal FEM simulations. This approach enables the derivation of meaningful simulation-ready 3D models from limited survey data.

1. Introduction

Masonry is one of the oldest and most enduring construction techniques and forms the backbone of countless worldwide cultural heritage (CH) buildings. Masonry digitalization and segmentation processes, recently enriched with Machine and Deep Learning (ML/DL), enable precise structural analyses and interpretations, enhancing CH preservation through advanced digital workflows.

The analysis of heritage buildings for structural health or thermal performance presents unique challenges. Indeed structural diagnostics (Michael et al., 2024), energy efficiency (Cespedes-Cubides and Jradi, 2024), and real-time simulation (Xiong et al., 2024), require careful adaptation to the complexity and historical sensitivity of heritage sites. These approaches often rely on mesh-based 3D models and benefit from standardized file formats that support interoperability and scalability, yet they face challenges in accuracy and data processing. A primary challenge in this domain is the geometric complexity of heritage buildings. Their irregular and often deteriorated shapes make accurate 3D modelling particularly challenging. While traditional Building Information Modeling (BIM) tools offer powerful solutions for modelling regular structures, they struggle to capture the organic, non-standard shapes typical of historical architecture. Furthermore, CH buildings often lack comprehensive surveys, including essential inspections, structural assessments, and diagnostic tests or material analyses, which are crucial for informed conservation and restoration efforts.

1.1 Objectives and data

This work investigates the use of DL solutions to support and enhance finite element modelling (FEM) in cultural heritage applications. By leveraging AI-driven methods for automated feature extraction, modelling and analysis, this research introduces solutions optimized for a 3D FEM, enabling high precision in energy simulations. Non-geometric features for the FEM and thermal analyses are deduced, deriving this information directly from reality-captured data. By working with images and point clouds, we infer material-related information, such as masonry texture, to extract insights relevant to thermal performance. While the integration of real-world data in structural FEM is well explored, its application in energy or thermal modelling remains relatively underdeveloped.

Therefore, the aim of this paper is twofold:

1. to apply DL networks for extracting material-related information from visual data;
2. to present a workflow that derives semantically enriched meshes suitable for the energy analysis of CH buildings.

Figure 1. 3D reality-based survey of the Pretorio Palace in Trento (IX-XIII century), Italy.

The implemented methodology is tested on the Palazzo Pretorio in Trento, Italy (Figure 1). The 3D survey of the building (Barbini et al., 2024) comprises 1080 photogrammetric images and 172 terrestrial laser scanner (TLS) scans. The scans cover both indoor and outdoor environments and were acquired with a

https://doi.org/10.5194/isprs-annals-X-M-2-2025-301-2025 | © Author(s) 2025. CC BY 4.0 License.

Faro Focus S120, whereas images were captured with a DJI Mavic 2 Pro (aerial imagery) and a Sony Alpha 6000 (ground-based image capture). Image and range data were processed and integrated to create a colorized point cloud of about 50 mil. points. Orthophotos of the eastern and western façades used for the reconstruction were generated from a photogrammetric survey using a Sony Alpha6000 DSLR mounted on a 9 m telescopic pole.

2. Related works

Recent developments in structural or energy monitoring for CH structures increasingly leverage advanced sensing technologies and AI-based techniques. 3D scanning has been widely employed for displacement tracking (Moon and An, 2024), and integrating reality-based measurements in the mesh modelling process further enhances accuracy in the displacement detection (Zhang et al., 2023). Recent work on controllable mesh generation using diffusion models has enabled fine-grained, high-quality mesh synthesis (Lyu et al., 2024), while related approaches address multi-view inconsistencies in textured meshes through optimized alignment and stitching (Zhao et al., 2024; Zheng et al., 2024). AI-based solutions for 3D reconstruction (such as Neural Radiance Field – NeRF) have also been recently tested and assessed for the CH context (Mazzacca et al., 2023; Murtiyoso et al., 2024; Haitz et al., 2024).

In parallel, DL methods have also emerged for detecting masonry wall patterns (Forster et al., 2023) or identifying damage using transformer models with YOLO (Idjaton et al., 2022).

Structural analysis spans applications including rubble masonry interventions (Valero et al., 2018), FEM modelling of brick walls (Ahiwale et al., 2023), TLS-FEM integration for tunnel deformation monitoring (Yang et al., 2022), and timber structure analysis (Özkan et al., 2025). FEM techniques are increasingly being integrated with point cloud-based models to improve the accuracy of deformation and stress analysis in bridges (Matono and Nishio, 2024).

2.1 Meshes for FEM analysis

FEM is a numerical technique used to solve Partial Differential Equations (PDEs) by discretizing a spatial domain Ω into finite elements (Liu and Glass, 2013). These elements, such as triangles and rectangles (2D) or tetrahedrons and hexahedrons (3D), form a mesh, which is a non-overlapping tessellation of the domain Ω. Solutions are computed at nodes or within domain elements, using shape functions to interpolate displacement, strain, and stress. Each element contributes to the global system, ensuring solution continuity across the domain (Kutlu and Soyluk, 2024). Meshes for structural analysis are commonly generated from manually developed CAD or BIM models (Zou et al., 2024a; Zou et al., 2024b), with IFC files acting as a widely adopted neutral and structured format. A watertight, clean geometry, free from gaps and overlaps, is crucial for producing valid surface or volume meshes, particularly in solid or nonlinear simulations.

As reported in Liu and Glass (2013), denser and more accurate meshes improve Finite Element Analysis (FEA) results but require increased computational time and resources. To effectively use FEM models for analyses on buildings, such as structural or thermal simulations, the building geometry must be (Zou et al., 2024a):

- Discretized into elements (planar or volumetric meshing).
- Conforming, in the sense that all adjacent elements must share faces without any gaps.
- Enriched with appropriate material properties (e.g., shear resistance, thermal conductivity, reflectance).

3. Methodology

The proposed methodology combines geometric and semantic information extracted from images and point clouds. It integrates masonry patterns from image analysis with spatial information from 3D point clouds to enable a data-driven unified interpretation of spatial and contextual information of masonry elements. The proposed workflow is summarized in Figure 2, with the orthoimage of the façades used for the extraction of the masonry pattern and the TLS point cloud for deriving wall thickness. Then, information is merged to generate an adaptive mesh model. The key points of the pipeline are:

1. *Object detection in image tiles*. Masks are extracted with YOLO network to identify architectural elements, such as stone blocks and mortar joint (Section 3.1).
2. *Wall thickness values extraction from the 3D point cloud.* Based on the extracted stone masks, a FEM model is generated from vectorized patterns. The point cloud is then voxelized to compute thickness values per voxel (Section 3.2).

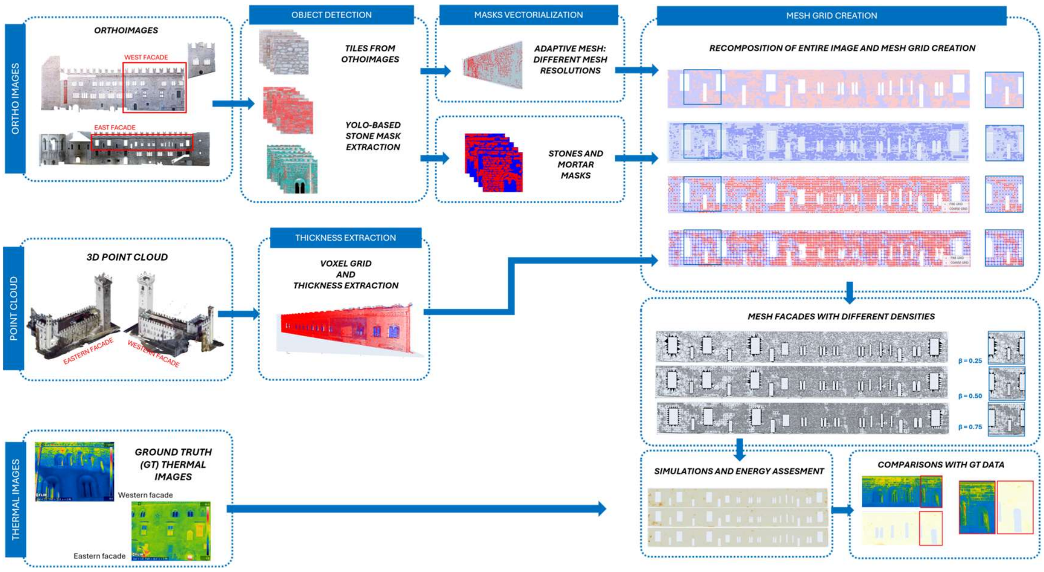

Figure 2. General workflow for 2D and 3D data processing and comparison with ground truth thermal data.

3. *Mesh grid creation and downsampling.* Mask polygons (point 1) are vectorized to generate a density pattern, which is refined based on both the mask classification and wall thickness, denser in stone regions and coarser in mortar areas. Stone zones identified in pixel-based images lead to finer meshes, while mortar regions result in simplified ones. A grid is overlaid on the previous pattern, and a parameter β controls point downsampling to define varying mesh densities (Section 3.3).
4. *Evaluation of thermal analysis for FEM.* Thermal analysis is conducted using meshes with varying levels of density, and the resulting temperature distributions were validated against ground truth (GT) thermal imagery (Section 3.4).

Each key step is further explained in the next paragraphs.

3.1 YOLO mask extraction

Starting from orthoimages of the main facades of the Palace (Section 1.1), we extracted 640×640 pixel tiles from the RGB datasets. A DL model based on the YOLOv7 architecture was trained to detect and segment individual stones (Figure 3) and separate them from mortar. The network was trained using a dataset of 203 annotated images.

Polygons are extracted from the image masks detected by YOLO in order to compare the results of the DL detection with the manually generated GT masks. To eliminate redundant and overlapping bounding boxes, a Non-Maximum Suppression (NMS) algorithm is applied. This technique selects the bounding box with the highest confidence score and suppresses all other boxes whose Intersection over Union (IoU) exceeds a predefined threshold (IoU > 0.55).

3.2 Thickness extraction

In parallel, the TLS point cloud is processed using the methodology outlined by Roman et al. (2024), yielding classification results that are consistent with those reported in that study. Normals are computed for the classified walls, and the DBSCAN algorithm is applied to distinguish between internal and external wall surfaces. The 3D point cloud is voxelized at a resolution of 0.50 m, in order to balance geometric detail with manageable computational demands. For each voxel, the best-fitting planes of the internal and external wall surfaces are computed, and the wall thickness (th_w) is estimated as the distance between them (Fig 4).

To augment the YOLO-derived vectorized mask patterns (P_{YOLO}) with geometric context, each vertex of the mask polygons is assigned the thickness value of the nearest voxel to which it belongs.

The point cloud coordinates, YOLO mask vertices, and voxel centroids are then defined as follows (Eq. 1, Eq. 2, Eq.3):

$$P_{las} = \{p_i = (x_i, y_i, z_i) \mid i = 1, \ldots, N\} \qquad \text{(Eq. 1)}$$

$$P_{Yolo} = \{p'_j = \left(u_j, v_j, w_j\right) \mid j = 1, \ldots, M\} \qquad \text{(Eq. 2)}$$

$$P_{vox} = \{v_k = \left(v_x, v_y, v_z\right) \mid k = 1, \ldots, L\} \qquad \text{(Eq. 3)}$$

The RANSAC plane-fitting algorithm is applied separately to the internal and external surfaces of P_{las} to estimate the main reference planes for the wall. Additionally, RANSAC is applied at the voxel level to fit local planes of internal and external surfaces within each voxel, enhancing accuracy.

For each voxel centroid P_{vox}, the Euclidean distance between the locally fitted internal and external planes is then computed, representing the local wall thickness ($th_{w,vox}$), as shown in Eq. 4.

$$th_{w,vox} = || p_{int} - p_{ext} || \qquad \text{(Eq. 4)}$$

Figure 3. Example of YOLO mask extraction with confidence value (left) and only masks (right).

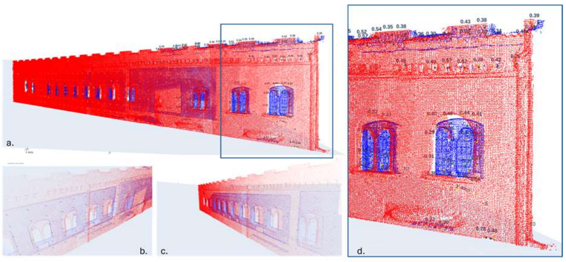

Figure 4. Wall surfaces and local thickness ($th_{w,vox}$) values extracted.

YOLO mask vertices are then reprojected onto the main 2D vertical plane, embedding thickness data. Each vertex is defined by:

- Voxel centroid reference (P_{vox}).
- Vectorized mask vertices (P_{YOLO}).
- Local wall thickness value ($th_{w,vox}$).

3.3 Finite Element Model from masks

To generate the data-driven parametric mesh, all vectorial masks are first extracted from the YOLO-processed image tiles and used to reconstruct a comprehensive mask for the entire input image.

A binary depth map is then produced to highlight areas with a higher density of detected stones (Figure 5).

This map effectively distinguishes regions with more pronounced masonry textures, as well as blue-shaded areas indicating greater concentrations of mortar or small, not-detected stones. The resulting binary map provides a clearer and more effective visualization of these regions.

Mesh parameterization starts with an initial uniform grid generated according to the average dimensions of the detected mask patterns.

This base grid is then adaptively refined using data-driven criteria to balance geometric accuracy and computational efficiency:

- In regions marked with a red mask, indicating stone texture, the grid is locally refined by reducing cell size in all directions, enabling higher-resolution representation of complex surfaces.
- Conversely, in blue mask regions, indicating little or no stone texture, the grid is coarsened by enlarging cells in all directions, simplifying low-detail areas.
- Where windows are present, the mesh is absent.

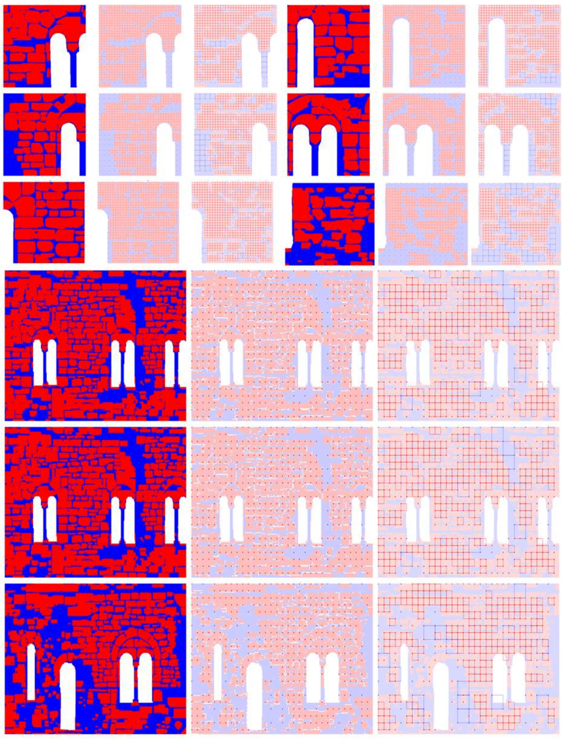

Figure 5. Masks (on the left) localizing stones (red masks), mortar (blue masks) and windows (white masks) adaptive grid data-driven (on the right).

Grid size is also modulated based on thickness values: it is reduced in regions where the local thickness values exceed the 90th percentile of all the thickness values and increased where it falls below the 10th percentile. For intermediate thickness values, the original grid resolution is maintained.

These steps are illustrated in Figure 6: (a) the reconstructed binary map; (b) adaptive vertices grid with computed intersections; (c) grid vertices classified as stone or mortar; and (d) the resulting adaptive mesh.

Finally, the parameter β is introduced to control the density of vertices within the grid.

This parameter selectively downsamples the internal vertices while preserving those located along boundaries and around window openings. The resulting vertices pattern serves as the basis for mesh triangulation. While a higher mesh resolution improves the accuracy and quality of simulation results, it also significantly increases the computational load and file size.

Three mesh densities were defined, retaining respectively 25%, 50%, and 75% of vertices controlled by the parameter β.

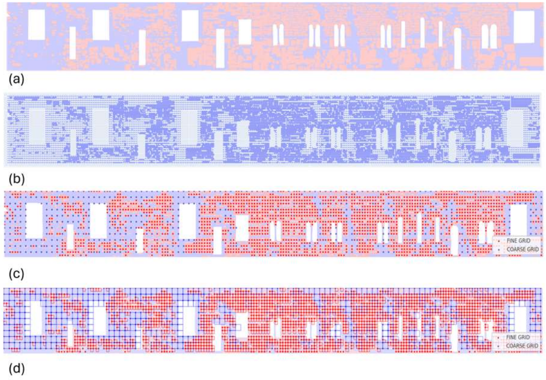

Figure 6. Workflow for data-driven adaptive mesh generation.

3.4 FEA analysis

The objective is to analyse how the density of a data-driven mesh influences thermal performance simulations. This investigation is based on the underlying assumption of differing thermal properties between mortar joints and stone textures.

As illustrated in Figure 7, thermal transmittance is notably higher in the mortar regions compared to the stone, confirming this premise. The thermal imagery clearly demonstrates that areas composed predominantly of stone exhibit superior thermal insulation properties relative to those consisting primarily of mortar.

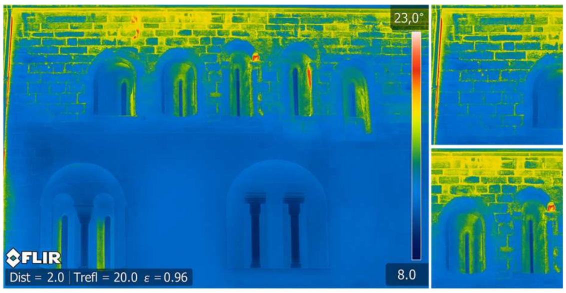

Figure 7. Thermal image used as GT for further simulations.

Thermal analysis used outdoor conditions matching the thermal imaging day, with a fixed indoor temperature set by standards to simulate wall heat transfer. The U-value was set at 3.2 W/m²K, based on wall thickness from point cloud data and aligned with similar buildings in the area. Each mesh was processed by extracting vertices, triangular faces, and surface areas. Heat transfer intensity Q for each triangle was calculated using (Eq. 5):

$$Q = U \cdot A \cdot \Delta T \qquad \text{(Eq. 5)}$$

where U denotes the overall heat transfer coefficient (thermal transmittance), A is the area of the triangular face, and ΔT the temperature difference across the wall, representative of the indoor-outdoor difference in thermal conditions.

4. Results

The evaluation of the presented methodology is structured around three main components: (1) object detection performance using the in-house pre-trained model YOLOv7, with visual and quantitative results on tiles; (2) mesh quality generation across density variations; and (3) thermal simulation outputs.

The next sections report the proposed workflow (Figure 2) applied to the third floor of the eastern and western façades.

4.1 YOLO masks evaluation

To quantitatively assess detection performance, the predicted mask polygons generated by the YOLOv7 network are compared against manually annotated GT masks. The following evaluation metrics are computed (Eq. 6, Eq. 7, Eq. 8):

- *Intersection over union (IoU):*

$$IoU = \frac{\text{Area of Intersection}}{\text{Area of Union}} \qquad \text{(Eq. 6)}$$

- *F1 score:*

$$F1 = \frac{2 \times |A \cap B|}{|A| + |B|} \qquad \text{(Eq. 7)}$$

- *Precision:*

$$\text{Precision} = \frac{\text{True Positive}}{\text{True Positive} + \text{False Positive}} \qquad \text{(Eq. 8)}$$

The Hungarian algorithm matches GT and YOLO polygons by IoU, discarding pairs below 2 cm, 5 cm, or 10 cm thresholds. Table 1 report results of the YOLO masks extraction for some tiles, compared with the manual annotated ones, at 5 cm.

# tile	*Matched pairs*	*Average IoU*	*Average F1*	*Average Precision*
east_tile_0008	74	0.58	0.94	0.91
east_tile_0009	92	0.68	0.97	0.96
east_tile_0010	57	0.69	0.94	0.90
east_tile_0012	62	0.66	0.97	0.95
west_tile_0000	13	0.62	0.82	0.74

Table 1. Results for some tiles at $th = 0.05$.

As shown in Figure 8, larger, regularly shaped stones, especially in window and door frames, are not effectively detected due to their geometric regularity, which contrasts with the irregular stone patterns the model has predominantly been trained on, leading to reduced detection confidence.

Similarly, elongated stone slabs near the upper portions of the wall are frequently missed, likely due to their atypical aspect ratios falling outside the model's learned shape distribution.

In contrast, irregularly shaped stones that constitute the main body of the wall are effectively detected by the YOLO model.

Quantitative evaluation against the GT shows that detection performance improves with tolerance thresholds, achieving an average precision of 0.69 at a 2 cm tolerance, 0.84 at 5 cm, and 0.98 at 10 cm.

These results confirm the network’s robustness in identifying irregular masonry units while also highlighting its limitations in handling geometrically uniform or atypically proportioned elements relative to the data it was trained on.

The evaluation metrics are summarized in Table 2, while visual detection results for a selection of tiles are presented in Figure 9. Additionally, Figure 9 shows two examples, where red outlines indicate the manual ground truth (GT) and blue outlines represent YOLO predictions, highlighting some limitations of the YOLO model in terms of:

1. *Detection of elongated stones (green)*: The model underperforms with long/narrow stones due to training data biased toward irregular shapes with standard aspect ratios.
2. *Shape simplification (red):* Regular or symmetric stones are sometimes oversimplified, resulting in masks that don't fully capture their contours.
3. *Aggregation of small stones (yellow)*: Regular or symmetric stones are sometimes oversimplified, resulting in masks that don't fully capture their contours.
4. *Difficulty with regular-shaped stones (blue):* Regular or symmetric stones are sometimes oversimplified, resulting in masks that don't fully capture their contours.

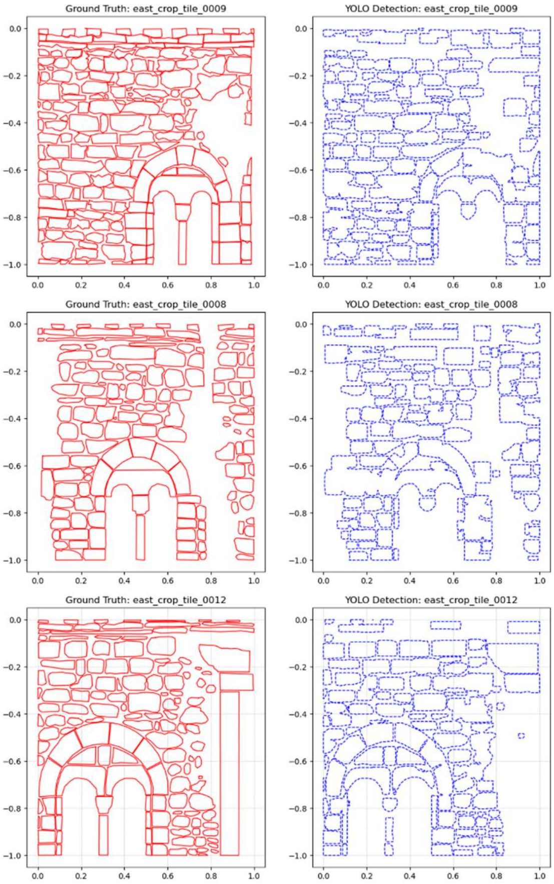

Figure 8. Comparison between GT data (left) and YOLO extracted masks (right).

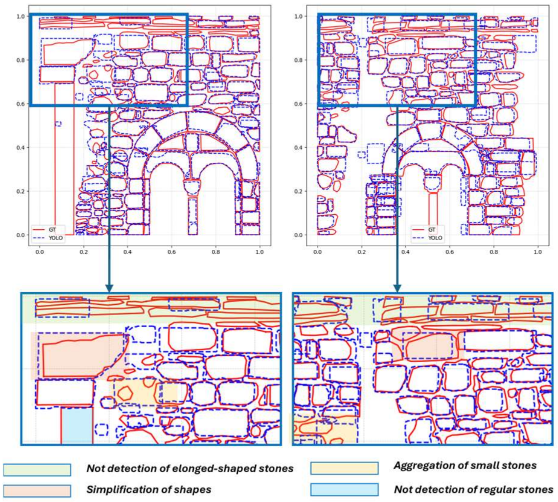

Figure 9. Inaccuracies of YOLO masks extraction.

4.2 Adaptive mesh generation

To assess reconstruction fidelity and mesh efficiency, two meshing strategies were applied to three façade sections: (a) 3rd East Floor, (b) West Façade, and (c) 3rd West Floor. Figure 10

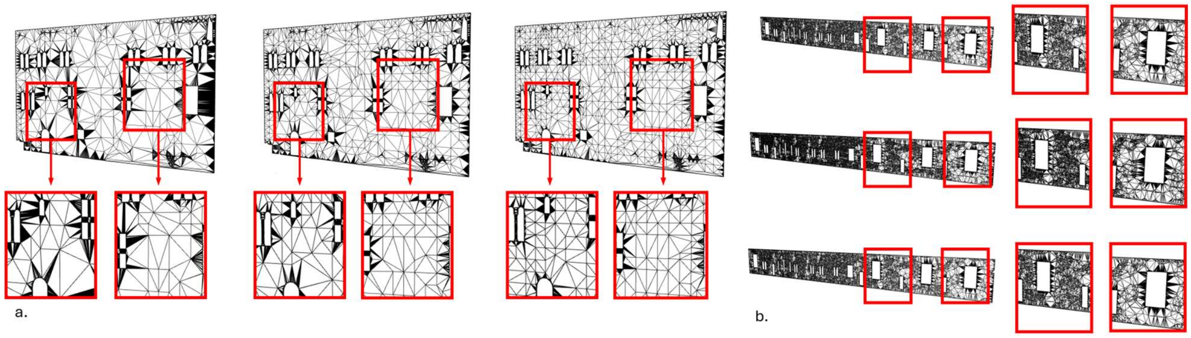

Figure 10. Mesh density visualization for the entire west façade (left) and the third floor of the eastern façade (right).

shows the proposed method’s ability to retain structural features and embed thickness metadata while reducing data complexity.
Figure 11 compares vertex (bars) and face (lines) counts generated by Method 1 and the proposed Method 2 across the three segments. Method 1 projects the point cloud onto a vertical plane, applies subsampling at β_{25}, β_{50}, and β_{75} levels, and uses Delaunay triangulation. Method 2 integrates YOLO-based semantic segmentation with adaptive meshing, yielding lighter, semantically rich models.

Threshold [m]	***Average IoU***	***Average F1***	***Average Precision***
0.02	0.53	0.61	0.70
0.05	0.66	0.74	0.84
0.10	0.84	0.99	0.98

Table 2. YOLO mask extraction metrics at three threshold levels.

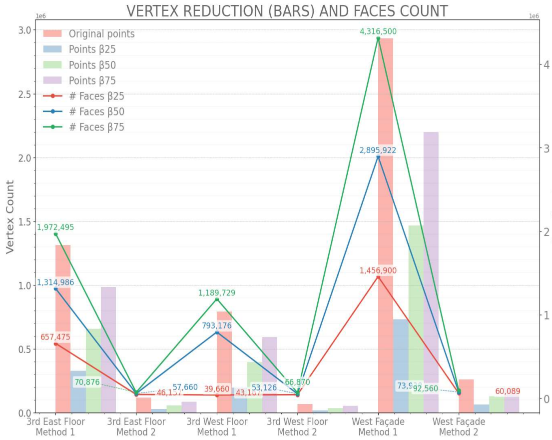

Figure 11. Point and face count comparison between Method 1 and proposed Method 2 across varying β values.

Results show Method 1 preserves more geometry but at higher computational cost, while Method 2 achieves major reductions, particularly at β_{50} and β_{75}, without compromising key features. The dual-axis graph underscores Method 2’s ability to produce efficient, simulation-ready models. Notably, no standardized benchmarks currently exist for evaluating mesh quality in the context of energy analysis.
The resulting meshes support thermal simulations.
While surface area (A) and total heat transfer (Q) stay constant, heat distribution depends on the decimation parameter β. Higher β produces finer meshes with more accurate gradients; lower β yields coarser meshes with less spatial detail.

4.3 FEM simulations

Figure 12 illustrates mesh density variations for Method 1 (a–c) and the proposed method (d–f) across different β levels, evaluated under thermal simulation settings using the parameter framework from Section 3.4 and Equation 5. Each pair (a–d, b–e, c–f) enables direct comparison of the same detail at equivalent resolution between the two methods.

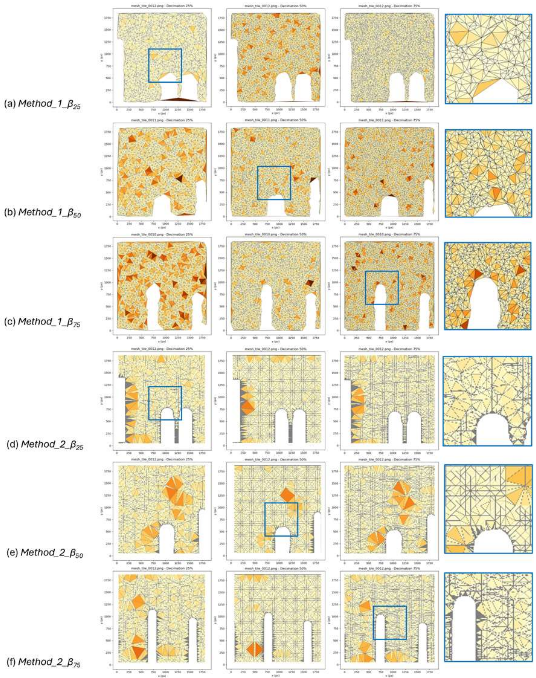

Figure 12. Mesh comparison between Method 1 (a-c) and the proposed Method (d-f) across β_{25}, β_{50}, β_{75}.

Despite simplification, the proposed method maintains the accuracy needed for thermal applications, also by embedding thickness metadata, achieving a balance between geometric reduction and fidelity.

4.4 FEM analysis and evaluation

Thermal analysis on all meshes obtained with the presented method confirms accurate representation of global heat transfer despite reduced detail. Areas of energy loss, such as thickness transitions, remain detectable. Simulation accuracy depends on mesh density (β) and spatial material encoding. In the East façade (Figure 13), β-sampled meshes preserve key thermal gradients, notably between stone units and mortar joints, consistent with ground truth thermal patterns.

As explained in Section 3.6, simulation parameters replicate real acquisition conditions. The temperature labels in Figure 13 confirm alignment between simulated and observed thermal behaviour, validating the method’s reliability for thermographic analysis under decimated, semantically enriched meshing. This validates the method’s suitability for thermographic evaluation under geometric simplification.

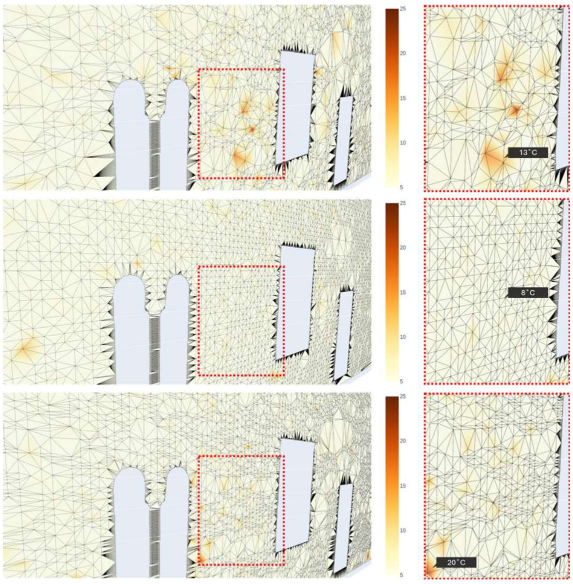

Figure 13. Thermal simulations at different mesh resolutions with the presented method, and output temperatures.

Figure 14 shows the proposed pipeline applied to West façade, starting from the original image, followed by YOLO mask outputs, and thermographic analysis highlighting key anomalies. The lower rows show progressively simplified, semantically guided meshes (β = 0.25, 0.50, 0.75), effectively preserving structural details. Coloured boxes link details and features across views, showing consistency and interpretability of the results.

Regarding the same façade (Figure 15), two detailed areas, labeled (A1) and (A2), are presented to illustrate key outcomes of the thermal simulations. Detail (A1) focuses on the upper portion of the façade, where the masonry pattern was accurately detected and successfully incorporated into the mesh generation process. The simulated heat distribution in this region aligns closely with the reference thermal image, validating the reliability of the adaptive meshing approach in reproducing localized thermal behavior based on texture-informed segmentation. Moreover, detail (A2) demonstrates a key feature of the workflow: the integration of wall thickness during mesh construction.

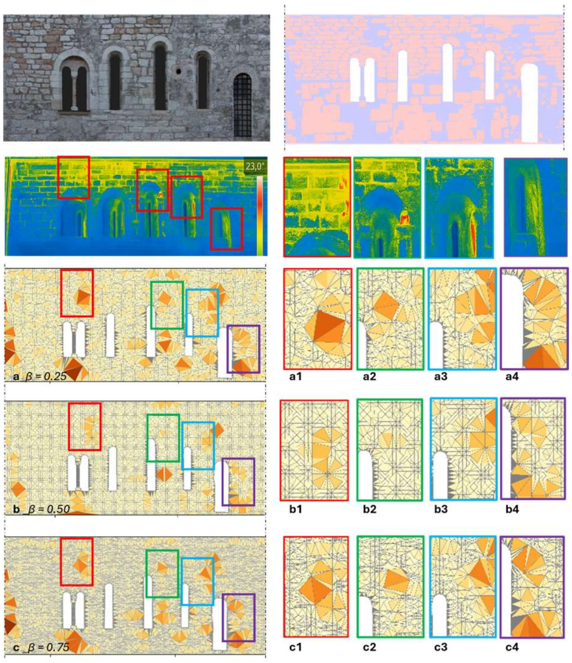

Figure 14. Multi-scale results of the proposed method at β_{25} (a), β_{50} (b), and β_{75} (c). Insets (a1–c4) show consistent thermal and geometric feature preservation across decimation levels.

In this case, a bricked-up window, barely distinguishable visually, is captured through voxel-based point cloud analysis due to a localized reduction in wall thickness.

This variation is automatically embedded in the FEM mesh, and the simulation correctly predicts increased thermal dispersion in the thinner region, confirming the impact of geometric parameters on heat transfer simulation.

These results underscore the proposed method’s value in CH thermal diagnostics, as it fuses visual, geometric, and semantic data to enhance mesh fidelity and improve thermal analysis reliability.

5. Conclusions

This work presented an integrated, data-driven workflow combining DL, 3D point cloud processing, and adaptive meshing to support CH monitoring and energy analysis. By combining DL and numerical simulations, the reported framework presents a breakthrough for the thermal analysis and simulations of heritage

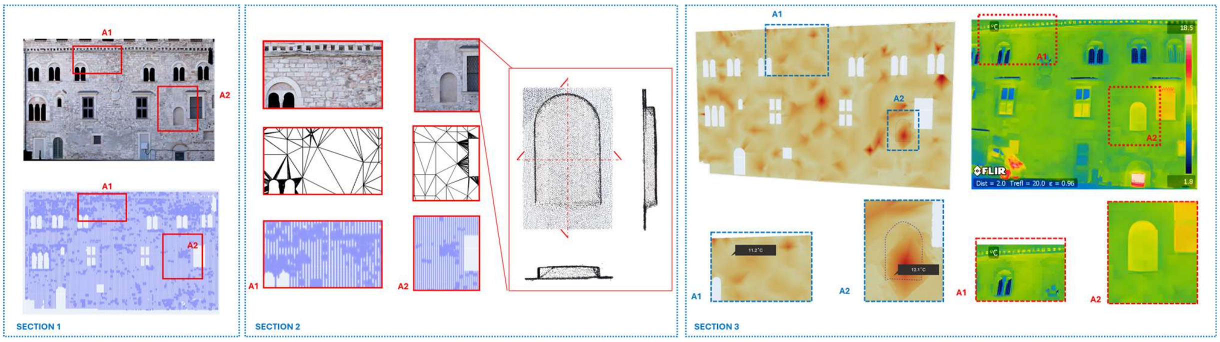

Figure 15. Western façade: adaptive mesh reconstruction (Section 1), focus on the bricked-up window (Section 2), simulation highlighting the bricked-up window and comparison with thermal image (Section 3).

buildings. The image segmentation model effectively identified irregular masonry, achieving average precision from 0.68 (2 cm tolerance) to 0.98 (10 cm). Limitations were observed with regular elements (e.g., lintels, jambs) due to divergence from the training set. High F1 scores (>0.90) validate robust pattern detection via IoU thresholds. Adaptive meshing for FEM analysis, driven by segmentation and thickness inputs, balanced detail and performance, as shown in the close outputs' temperatures obtained, while the β parameter enabled controlled simplification while preserving structural and thermal reliability. Future work includes enhancing detection of regular units, automating material inference from texture, and integrating time-series data for predictive CH diagnostics.

References

Ahiwale, D.D., Kontoni, D.-P.N., Jadhav, A.V., Bawale, A.B., 2023. FEM analysis of the effect of various brick bond patterns on masonry walls under in-plane cyclic loading. *Asian Journal of Civil Engineering*, 24(7), pp. 2629–2643.

Barbini, A., Giampiccolo, F., Maragno, A., Massari, G.A., Pellegatta, C., 2024. Innovation and Tradition: Integrated Practices in the Architectural Survey of Pretorio Palace in Trento. *SCIRES-IT*, 14(1), pp. 45–62.

Cespedes-Cubides, A.S., Jradi, M., 2024. A review of building digital twins to improve energy efficiency in the building operational stage. *Energy Inform 7*, 11.

Forster, A., Valero, E., Bosché, F., Hyslop, E., Wilson, L., 2023. Digital Toolkit to Assist the Interpretation of Traditional Masonry Construction. *Int. Jour. of Arch. Her.*, *18*(5), 725–739.

Haitz, D., Kıvılcım, B., Ulrich, M., Weinmann, M., Weinmann, M., 2024. Density-based Geometric Convergence of NeRFs at Training Time: Insights from Spatio-temporal Discretization. *Int. Arch. Phot. Rem. Sens. Spat. Inf. Sci., XLVIII-2/W7-2024,* 49–56.

Kutlu, I., Soyluk, A., 2024. A comparative approach to using photogrammetry in the structural analysis of historical buildings. *Ain Shams Engineering Journal*, 15(1), 102298.

Idjaton, K., Desquesnes, X., Treuillet, S., Brunetaud, X., 2022. Transformers with YOLO Network for Damage Detection in Limestone Wall Images. Proc. *Image Analysis and Processing – ICIAP 2022 Workshops*, LNCS, Vol. 13374, pp. 302-313.

Liu, Y., Glass, G., 2013. Effects of Mesh Density on Finite Element Analysis. *SAE Technical Paper* 2013-01-1375.

Lyu, Z., Fei, B., Wang, J., Xu, X., Zhang, Y., Yang, W., Dai, B., 2024. GetMesh: A Controllable Model for High-Quality Mesh Generation and Manipulation. *arXiv preprint*, arXiv:2403.11990.

Matono, G., Nishio, M., 2024. Component-level point cloud completion of bridge structures using deep learning. *Computer-Aided Civil and Infrastructure Engineering*, 39, 2581–2595.

Mazzacca, G., Karami, A., Rigon, S., Farella, E. M., Trybala, P., Remondino, F., 2023. NeRF for heritage 3D reconstruction. *Int. Arch. Phot. Rem. Sens. Spatial Inf. Sci.*, XLVIII-M-2-2023, 1051–1058.

Michael, J., Blankenbach, J., Derksen, J., Finklenburg, B., Fuentes, R., Gries, T., Hendiani, S., Herlé, S., Hesseler, S., Kimm, M., Kirchhof, J.C., Rumpe, B., Schüttrumpf, H., Walther, G., 2024. Integrating models of civil structures in digital twins: State-of-the-Art and challenges. *Journal of Infrastructure Intelligence and Resilience*, 3(3), 100100.

Moon, S.H., An, D.W., 2024. Measuring Displacement before and after Repair on Korean Wooden Built Heritage: Records for Authenticity and Sustainability. *Sustainability*, 16, 1101.

Murtiyoso, A., Markiewicz, J., Karwel, A. K., Grussenmeyer, P., Kot, P., 2024. Comparison of state-of-the-art multi-view stereo solutions for close range heritage documentation, *Int. Arch. Phot. Rem.Sens. Spatial Inf. Sci., XLVIII-2/W4-2024*, 317–323.

Özkan, T., Lavric, I., Hochreiner, G., Pfeifer, N., 2025. Automated 3D Modeling vs. Manual Methods: A Comparative Study on Historic Timber Tower Structure Assessment. *Remote Sens. 17*, 448.

Roman, O., Bassier, M., De Geyter, S., De Winter, H., Farella, E. M., Remondino, F., 2024. BIM Module for Deep Learning-driven parametric IFC reconstruction, *Int. Arch. Photogramm. Remote Sens. Spatial Inf. Sci., XLVIII-2/W8-2024*, 403–410.

Valero, E., Bosché, F., Forster, A., 2018. Automatic segmentation of 3D point clouds of rubble masonry walls, and its application to building surveying, repair and maintenance. *Automation in Construction*, 96, pp. 29-39.

Xiong, R., Shi, Y., Jing, H., Liang, W., Nakahira, Y., Tang, P., 2024. Calibrating subjective data biases and model predictive uncertainties in machine learning-based thermal perception predictions. *Building and Environment*, 247, 111053.

Yang, H., Xu, X., Xu, X., Liu, W., 2022. TLS and FEM combined methods for deformation analysis of tunnel structures. *Mechanics of Advanced Materials and Structures*, *31*(6), 1264–1271.

Zhang, J., Eisenträger, S., Zhan, Y., Saputra, A., Song, C., 2023. Direct point-cloud-based numerical analysis using octree meshes. *Computers & Structures*, 289, 107175.

Zhao, Z., Song, C., Gu, X., Dong, Y., Zuo, Q., Yuan, W., Bo, L., Dong, Z., Huang, Q., 2024. An Optimization Framework to Enforce Multi-View Consistency for Texturing 3D Meshes. *arXiv preprint*, arXiv:2403.15559.

Zheng, X.-Y., Pan, H., Guo, Y.-X., Tong, X., Liu, Y., 2024. MVD^2: Efficient Multiview 3D Reconstruction for Multiview Diffusion. *arXiv preprint*, arXiv:2402.14253.

Zou, X., Lo, S.B., Sevil`la, R., Hassan, O., Morgan, K., 2024a. The Generation of 3D Surface Meshes for NURBS-Enhanced FEM. *Computer-Aided Design*, 168, 103653.

Zou, Y., Hu, F., Yang, H., Cai, J., Pan, H., Zhang, Q., 2024b. Detailed Design of Special-Shaped Steel Structures Based on DfMA: The BIM-FEM Model Conversion Method. *Buildings*, *14*(5), 1320.